inorganics

MDPI

Article

A Magnetic Nanocarrier of Ciprofloxacin Used for Restraining the Growth of the Multidrug-Resistant *Pseudomonas aeruginosa*

Kleoniki Giannousi [1,*], Eleni Zouni [1], Nikolaos Grigoriadis [2,3], Ioannis S. Vizirianakis [2,4], Ilias M. Oikonomou [5,6], Valeria Nicolosi [5,6] and Catherine Dendrinou-Samara [1,*]

1 Laboratory of Inorganic Chemistry, Department of Chemistry, Aristotle University of Thessaloniki, 54124 Thessaloniki, Greece; elenazouni@gmail.com
2 Laboratory of Pharmacology, School of Pharmacy, Aristotle University of Thessaloniki, 54124 Thessaloniki, Greece; ngrigoria@pharm.auth.gr (N.G.); ivizir@pharm.auth.gr (I.S.V.)
3 Biogenea pharmaceuticals Ltd., 26th Oktovriou 43, LIMANI Center, 5th Floor—5.06, 54627 Thessaloniki, Greece
4 Department of Health Sciences, School of Life and Health Sciences, University of Nicosia, Nicosia 2417, Cyprus
5 CRANN and AMBER Research Centers, Trinity College Dublin, College Green, D02 PN40 Dublin, Ireland; oikonomi@tcd.ie (I.M.O.); nicolov@tcd.ie (V.N.)
6 School of Chemistry, Trinity College Dublin, College Green, D02 PN40 Dublin, Ireland
* Correspondence: klegia@chem.auth.gr (K.G.); samkat@chem.auth.gr (C.D.-S.)

Abstract: Ciprofloxacin (CPL) is an effective antibiotic against *Pseudomonas aeruginosa*. However, its use is limited by the emergence of multi-resistant strains. In this study, 8–15 nm manganese ferrite ($MnFe_2O_4$) nanoparticles, aminated and/or PEGylated, have been used as drug-delivery systems of CPL. The magnetic nanoparticles (MNPs) were prepared in the presence of the aliphatic amines octadecylamine (ODA), oleylamine (OAm), or PEG8000 to achieve the appropriate surface chemistry for the direct conjugation of CPL and drug loading into the PEG matrix, respectively. The primary MNPs proved to be biocompatible in calf thymus (CT)-DNA interaction studies, with binding constant values K_b in the range of 4.43–6.5 $\times$ 10^4 $(g/mL)^{-1}$. ODA as a coater gave rise to $MnFe_2O_4$ MNPs, with a high percentage of free amines that further allowed for the conjugation of 90.9% CPL, which gradually released via a non-Fickian anomalous transport motif. The 25.1% CPL that loaded in the PEGylated MNPs led to a partial transformation of the nanoflowers into more aggregated forms. The release profile, although steeper, is described by the same model. The isolated magnetic nanocarrier with a high content of CPL was evaluated for its antimicrobial activity against a multi-resistant strain of *P. aeruginosa* using an automated industrial instrument (BacT/ALERT®3D), and its molecular profile was outlined by studying its interaction with plasmid DNA (pDNA). The prototype use of BacT/ALERT®3D allows for the simultaneous screening of multiple samples, while it foreshadows the transition to a preclinical phase.

Keywords: magnetic nanocarrier; *Pseudomonas aeruginosa*; multidrug resistance

check for updates

Academic Editors: Guido Kickelbick, Jianqiang Yu, Yan Zhang and Sanjun Fan

Received: 10 December 2024
Revised: 24 January 2025
Accepted: 13 February 2025
Published: 16 February 2025

Citation: Giannousi, K.; Zouni, E.; Grigoriadis, N.; Vizirianakis, I.S.; Oikonomou, I.M.; Nicolosi, V.; Dendrinou-Samara, C. A Magnetic Nanocarrier of Ciprofloxacin Used for Restraining the Growth of the Multidrug-Resistant *Pseudomonas aeruginosa*. *Inorganics* **2025**, *13*, 58. https://doi.org/10.3390/inorganics13020058

Copyright: © 2025 by the authors. Licensee MDPI, Basel, Switzerland. This article is an open access article distributed under the terms and conditions of the Creative Commons Attribution (CC BY) license (https://creativecommons.org/licenses/by/4.0/).

1. Introduction

The emergence of antimicrobial resistance in clinical settings is a diachronic pandemic issue because it limits patient outcomes since it is correlated with the inadequate therapeutic approaches of many bacterial infections. According to the European Center for Disease Prevention (ECDC), in countries in the European Union and European Economic Area, more than 35,000 deaths are recorded each year due to infections caused by multidrug-resistant microbial strains [1]. Antibiotics administration still remains the preferred method

to treat these infections, even though it has been reported that their abuse is the primary cause of critical multidrug-resistant microorganisms [2]. Although it may be feasible to find novel antibiotics, there is no guarantee that their development will be able to catch up with the resistance development of the pathogen in the time required [3,4]. Among the several resistant strains of fungi, Gram-positive, Gram-negative aerobes, and anaerobic bacterial species, *Pseudomonas aeruginosa* is particularly vexing to clinicians [5]. *P. aeruginosa* has been recognized as an opportunistic pathogen that is the most common bacterium associated with nosocomial infections and ventilator-associated pneumonia [6] while demonstrating diverse mechanisms of antibiotic resistance, both innate and acquired [5].

Nanomaterials could be an alternative solution to that problem due to their enhanced physicochemical and biological properties [7,8]. Monometallic nanoparticles and their oxides are intensively explored for their use against infectious pathogens, since the therapeutic and blocking effects of their bulk counterparts are well known from ancient times [9]. Metallic NPs have strong penetrability, easy surface modification, and the advantages of durability and heat resistance. Their nano size results in more stable antimicrobial activity compared to antibiotics in cases of infections caused by intracellular bacterial species [10]. Those characteristics allow for the intracellular delivery of antibiotics which, combined with their inherent properties, exhibit bacterial cell membrane damage and induce oxidative stress. Meanwhile, intermetallic forms, such as bimetallic copper–zinc NPs, have been reported to have even better antibacterial properties due to their synergistic effects [11]. Moreover, the co-administration of metallic NPs with commercial antibiotics, as a modern strategy to kill resistant bacterial species, offers many advantages, such as cost reduction and easy synthesis [4,12]. Our research group has already evaluated the co-administration of antibiotics, such as meropenem and ciprofloxacin, with monometallic (CuO, ZnO NPs) and bimetallic nanoparticles (CuZn NPs) against multi-resistant strains of *Pseudomonas aeruginosa* [13]. The results highlight the specialized activity of nanoparticles on the mechanisms of antimicrobial resistance development, such as efflux pump systems, through which bacteria can remove antimicrobial agents and other toxic substances [14]. As carriers, metal-based nanomaterials have a strong potential against a range of pathogenic bacteria, including *Pseudomonas*, as shown by investigating gold NPs linked with gentamicin [15] or vancomycin [16]. Magnetic nanoparticles (MNPs) possess a prominent position in the field of nanomedicine [17], with clinical trials highlighting them as suitable contrast agents in MRI [18], while, at the same time, they are being used as drug carriers, enabling magnetic targeting and their application as theranostic agents [19]. Manganese ferrite ($MnFe_2O_4$) nanoparticles stand out compared to other MNPs, such as Fe_3O_4, γ-Fe_2O_3, $CoFe_2O_4$, and $NiFe_2O_4$, since they show higher magnetization, stronger imaging ability, and large relaxivity [20]. $MnFe_2O_4$ MNPs have been previously used by us as nanoplatforms of non-steroidal anti-inflammatory drugs [21], while they have been recently conjugated with chemotherapeutics and tested *in vitro* in 3D breast cancer cell cultures [22]. However, toxicity issues still overshadow their intriguing properties, and, for that reason, low concentrations and/or different capping agents are required to protect the metallic core from rapid dissociation. The organic agents, depending on their nature and the coverage motif, protect the inorganic core and give in the NPs a biocompatible "face". In doing so, $MnFe_2O_4$ MNPs with suitable surface characteristics could be used as carriers of antibiotics to target specific areas of microbial infection. Moreover, the administration of a single nanoformulation containing both MNPs and commercial antibiotics is expected to improve the biocidal properties via the introduction of new mechanisms of on-site action in bacterial cells, along with effective targeting and delivery that could increase the solubility and stability of drugs and minimize their side-effects and dosages [23].

Herein, based on our previous experience, $MnFe_2O_4$ NPs with a different surface chemistry have been synthesized by implementing the aliphatic amines octadecylamine (ODA) and oleylamine (OAm) or polyethylene glycol (PEG) 8000 as coating agents. Their different surface chemistry allows for the implementation of distinct functionalization methods, which result in variant percentages of drug loading/conjugation and differentiations in the drug release profiles. The newly synthesized MNPs were further used as the starting material to prepare the magnetic nanocarriers of the antibiotic ciprofloxacin (CPL). CPL belongs to fluoroquinolone antibiotics with carboxylate donors in the molecule, and thus allows for both the direct conjugation with MNPs that have free amines (ODA, OAm) and the loading into the matrix of PEGylated MNPs. CPL is commonly used against the opportunistic pathogen *P. aeruginosa*, while its mechanism of action involves inhibiting the replication of bacterial DNA [24,25]. However, its extensive use has led to rapidly increasing ciprofloxacin-resistant *P. aeruginosa* isolates [24]. The primary MNPs were assessed for their biocompatibility via DNA interaction studies, while the magnetic nanocarriers were carefully characterized before and after loading/conjugation with CPL. The different surface chemistry of the MNPs indeed affected the drug loading, while a diverse release profile of CPL was found. The magnetic nanocarriers with a higher percentage of CPL were further tested for the antimicrobial activity against the multi-resistant strains of *P. aeruginosa* by implementing, for the first time, an automated system, BacT/ALERT®3D, in order to be closer to clinical practice. BacT/ALERT®3D is a state-of-the-art automatic microbial detection system. Built on bioMérieux's patented colorimetric technology, it saves time, facilitates cross-training, and helps prevent errors, while demonstrating unsurpassed recovery in a wide range of organisms. It is currently used in identifying microbes in patients' samples, in sepsis and quality control testing, and in monitoring the presence or absence of microorganisms, including *P. aeruginosa* [26]. Beyond its clinical and industrial uses, this instrument raise hopes of conforming to the rapid rate of development of antimicrobial resistance, since it automatically measures a large number of samples over a period of several days, thus allowing for pharmacokinetic analyses. If the bacteria are present in the test sample, carbon dioxide is produced, as the microorganisms metabolize the substrates in the culture medium. When the growth of the microorganisms produces CO_2, the color of the sensor in the bottom of each culture bottle changes from dark to light. A light-emitting diode (LED) projects light onto the sensor, and the light reflected is measured using a photodetector. Since the microbial growth in the presence of nanoparticles has never been assessed using this instrument, for the ratification of the BacT/ALERT®3D in present usage, nanoparticles with known activity towards this strain have also been evaluated, specifically CuO, ZnO, and CuZn NPs, either alone or in the cocktail form (co-administration) with CPL, which have been previously tested using a Checkerboard assay [13], were implemented once again in order to validate the consistency of the method. The encouraging results were further boosted by analyzing their mechanisms of action in terms of their interactions with plasmid DNA (pDNA).

2. Results and Discussion

2.1. Synthesis and Characterization of the Magnetic Nanocarrier

The aliphatic amines, OAm and ODA, with almost the same MW and different conformation, bending, and linearity, respectively, were utilized to provide MNPs with an aminated surface in order to directly conjugate CPL as a carboxylate donor, whereas PEGylation was used as another approach for CPL loading into the PEG matrix. To achieve a high percentage of free amines, based on our previous reports [27,28], a modified preparation of the MNPs took place in solvothermal conditions in the sole presence of OAm ($MnFe_2O_4$@OAm NPs) or ODA ($MnFe_2O_4$@ODA NPs), while PEG ($MnFe_2O_4$@PEG NPs)

was used in a triple role (solvent, surfactant, reducing agent), also simplifying the manner of the synthetic procedure.

Figure 1a shows the XRD patterns of coated $MnFe_2O_4$ MNPs. In all samples, the peaks at about 2θ of 29.8°, 35.2°, 42.7°, 52.7°, 56.6°, and 61.7° correspond to (220), (311), (400), (422), (511), and (440) planes of the crystalline structure of the NPs, respectively. The existence of these characteristic peaks proves that the sample is consistent with Jacobsite syn space group Fd-3m of manganese ferrite (PDF 74-2403). Furthermore, the XRD analysis indicates the existence of the spinel ($MnFe_2O_4$) phase, and the peak at 21° is attributed to the crystallization of the surfactant. The average crystallite size of the samples was 12 ± 0.3, 7 ± 0.4, and 8 ± 0.4 nm for $MnFe_2O_4$@ODA, $MnFe_2O_4$@OAm, and $MnFe_2O_4$@PEG MNPs, respectively. The calculation was obtained by fitting the diffraction data with a pseudo-Voigt function (Jade6 Software). The FT-IR spectrum of $MnFe_2O_4$@ODA is included in Section 2.3, while the respective spectra of $MnFe_2O_4$@OAm and $MnFe_2O_4$@PEG are given in the Supplementary Information (Figure S1). The TGA curves are given in Figure 2b. In the case of $MnFe_2O_4$@OAm NPs (gray line), a total weight loss of 16% is recorded in the temperature range of 100–800 °C. The mass loss up to 100 °C can be attributed to the removal of the absorbed water molecules, while the next two steps of loss come from the carbon chains and amine groups. In particular, the carbon chains become decomposed from 200 to 450 °C, while the removal of the amine groups takes place at higher temperatures (600–750 °C). In the case of $MnFe_2O_4$@ODA NPs (black line), it is demonstrated that a double layer of ODA molecules reaches a final percentage of 66%, while the three-staged weight loss of PEGylated MNPs reaches 67% (red line). As far as magnetization is concerned, the corrected saturation magnetization values (M_s) were calculated as 54, 61, and 66 emu/g for $MnFe_2O_4$@ODA, $MnFe_2O_4$@OAm, and $MnFe_2O_4$@PEG, respectively (Figure 2c).

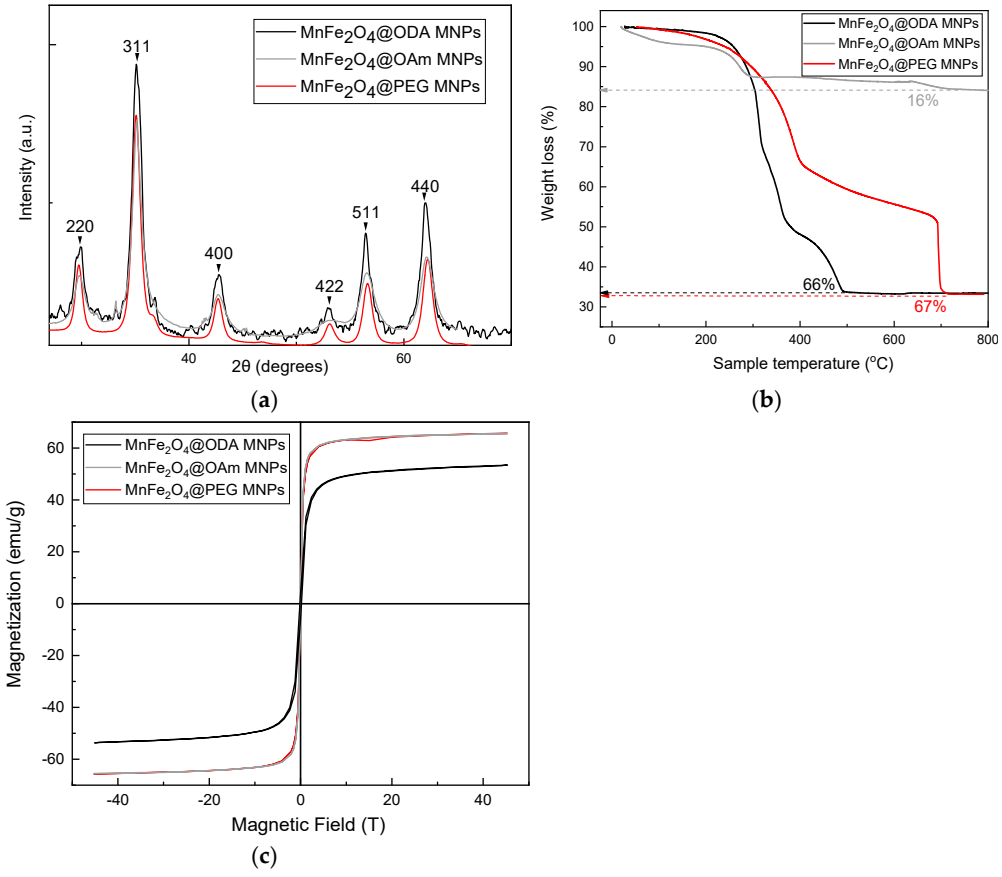


Figure 1. (**a**) XRD patterns, (**b**) TGA curves, and (**c**) VSM measurements of $MnFe_2O_4$@ODA, $MnFe_2O_4$@OAm, and $MnFe_2O_4$@PEG MNPs.

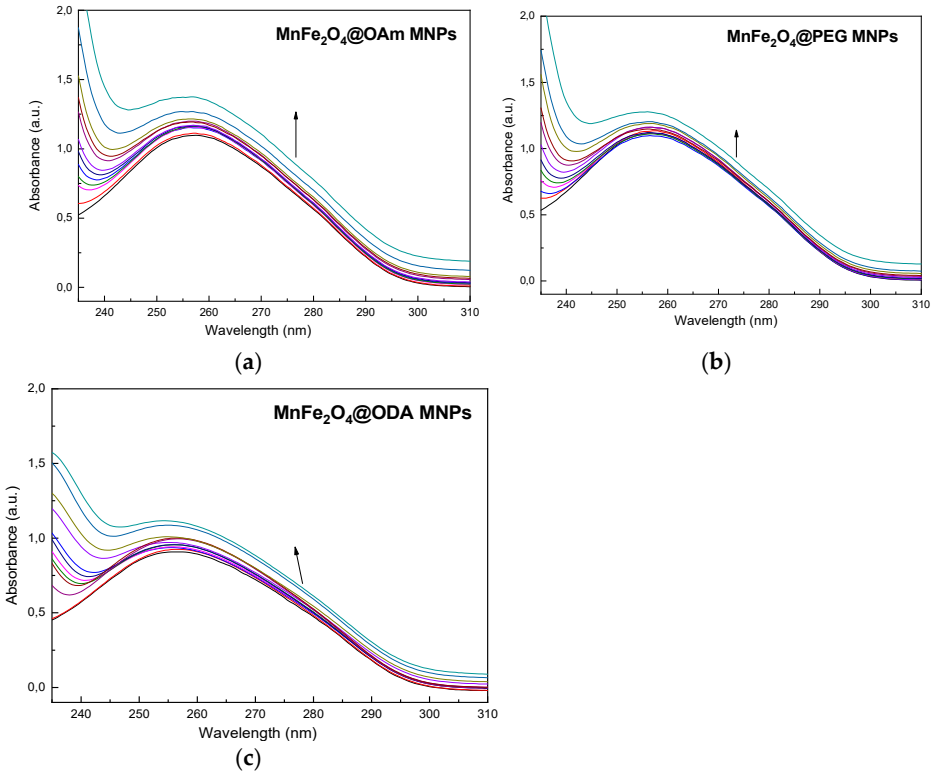


Figure 2. UV-vis absorption spectrum of CT-DNA (170 μM) alone at 260 nm and with increasing concentrations (0.6–17 μg/mL) of (**a**) $MnFe_2O_4$@OAm, (**b**) $MnFe_2O_4$@PEG, and (**c**) $MnFe_2O_4$@ODA MNPs.

The free -NH_2 on the surface of the MNPs prepared in the presence of amines were estimated using ninhydrin colorimetric analysis. ODA proved to be an effective capping agent in order to give rise to a large amount of free -NH_2. Specifically, the free -NH_2 for $MnFe_2O_4$@ODA MNPs were found to be 0.0207 mg/mL (82.8%), whereas for $MnFe_2O_4$@OAm MNPs, they were found to be 0.0189 mg/mL (7.6%). The colloidal stability of the primary MNPs was also under investigation. The hydrodynamic sizes of $MnFe_2O_4$@ODA, $MnFe_2O_4$@OAm, and $MnFe_2O_4$@PEG MNPs in terms of Z-average (d.nm) with the relative polydispersity indexes (PDI) were measured in 0.5% DMSO and found to be 106 nm (0.26), 60 (0.28), and 239 (0.26), respectively. The zeta potential values were found to be 39.7, 32.5, and 25.14 mV, respectively, which are indicative of stable colloidal suspensions.

2.2. Interaction of the Magnetic Nanocarriers with CT-DNA

The freshly prepared MNPs were initially tested for their interactions with calf thymus (CT-DNA) to evaluate their biocompatibility status. Typically, NPs bind to DNA through non-covalent interactions, which include intercalation, groove binding, and electrostatic interactions [29]. The conformational changes that may be observed in the DNA structure can be elucidated via UV-VIS spectroscopic studies. The method is based on the change or shift in the maximum absorbance of NPs or DNA observed during their interactions with each other. DNA absorbs UV light with wavelengths in the range of 257–260 nm due to the resonance structure of the purine and pyrimidine bases [30]. The alterations in the absorption spectrum of CT-DNA due to its interaction with the three different $MnFe_2O_4$ NPs are shown in Figure 2. A gradual increase in the intensity of absorbance is reported for $MnFe_2O_4$@OAm MNPs (Figure 2a), with significant hyperchromism for c > 9 μg/mL, whereas for the $MnFe_2O_4$@PEG MNPs (Figure 2b), the effect started to be more prominent from c = 6 μg/mL. In the case of $MnFe_2O_4$@ODA MNPs (Figure 2c),

the increase in the absorption of DNA is also observed in a concentration-dependent manner, but in concentrations higher than 9 μg/mL, a slight blue shift is recorded, probably indicating a partial destabilization of the double helix. Typically, hyperchromism occurs during the external binding of NPs into DNA through electrostatic interactions or binding in the major or minor grooves [31]. In the case of the presented MNPs, hyperchromicity is an indication of an electrostatic interaction, which is further confirmed by the zeta-potential and binding constants K_b values of MNPs. The K_b for $MnFe_2O_4$@OAm, $MnFe_2O_4$@PEG, and $MnFe_2O_4$@ODA NPs were calculated as 6.5×10^4, 4.8×10^4, and 4.43×10^4 $(g/mL)^{-1}$, respectively, based on Equation (1) (Figure 3).

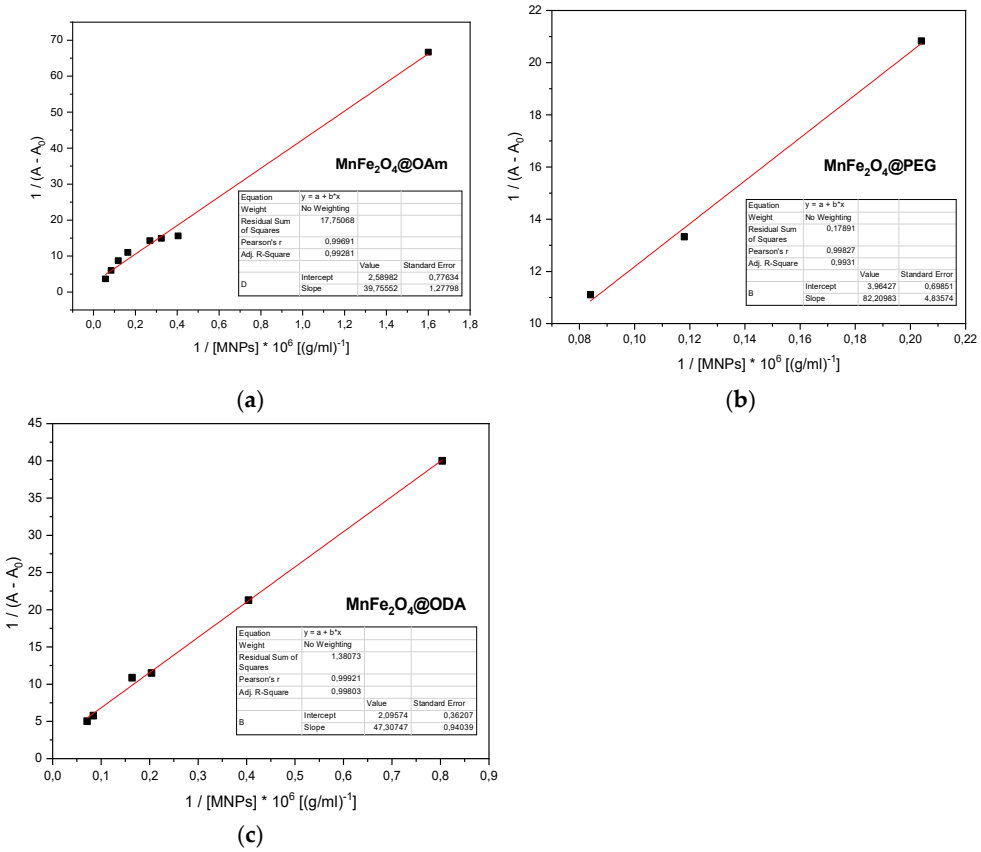


Figure 3. Plot of $1/(A\text{-}A_0)$ versus $1/[MNPs] \times 10^6$ for (**a**) $MnFe_2O_4$@OAm, (**b**) $MnFe_2O_4$@PEG, and (**c**) $MnFe_2O_4$@ODA.

This interaction mode via electrostatic forces is further supported by circular dichroism (CD) measurements. CD is commonly used to study the conformational changes induced in the structure of DNA upon interaction with MNPs. Non-covalent DNA-NPs interactions cause a change in the structure of DNA, resulting in an alteration of the CD spectrum [32]. CD of free helix DNA shows specific signatures of right-handed B form where a positive band at 275 nm due to base stacking and a negative band at 245 nm due to right-handed helicity is detected. Due to the interaction with MNPs, the structure of DNA can be stabilized or destabilized. Intercalation mode of binding can stabilize DNA structure and enhance the intensities of both the bands, whereas electrostatic interaction and groove binding show little or no perturbations on the two bands and destabilize the DNA's structure [33]. The CD spectrum of $MnFe_2O_4$@OAm MNPs, presented in Figure S2 (SI), shows that the intensity of the positive band of DNA decreases significantly after the addition of the MNPs, revealing that the binding of MNPs locally disrupts base stacking. Furthermore, an enhancement in the intensity of the negative peak is observed in combination with a slight bathochromic shift, indicating that the DNA helix is untwisted [34].

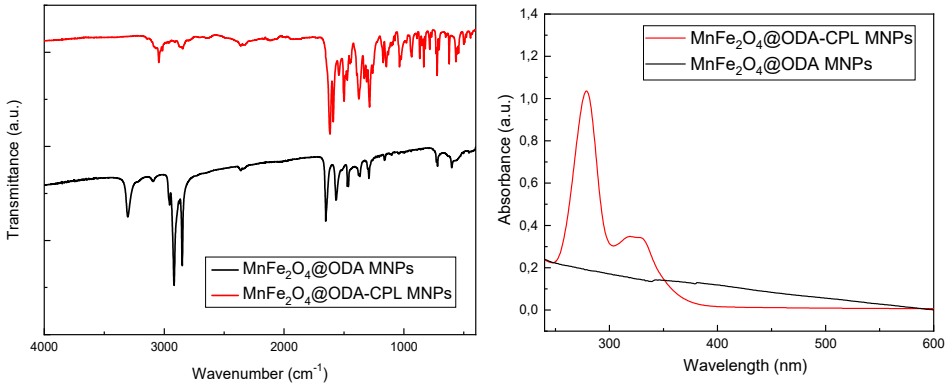
2.3. Direct Coupling of CPL with Aminated $MnFe_2O_4$ MNPs

$MnFe_2O_4$@ODA MNPs were selected among the aminated coated MNPs for the direct coupling of CPL, since they exhibited the highest percentage of NH_2 groups. The MNPs were conjugated with ciprofloxacin, via the formation of a covalent bond, through EDC-NHS chemistry, which was, at first, verified using FT-IR. The FT-IR spectrum of the nanoformulation $MnFe_2O_4$@ODA-CPL is presented in Figure 4a (red line) in comparison with that of the primary MNPs (black line), while the spectrum of neat ciprofloxacin is given in Figure S3 (SI). The black-lined spectrum confirmed the presence of ODA and free amines on the MNPs by the strong N-H stretching at 3300 cm^{-1} and the N-H wagging mode at ~728 cm^{-1} of ODA. At 2920 and 2850 cm^{-1}, the asymmetric and symmetric stretching vibrations of the methylene groups are observed, respectively. The peaks at 1470 and 1650 cm^{-1} are assigned to the bending vibrations of the -CH_2 and -NH_2 groups. Finally, in the 600–400 cm^{-1} region, the characteristic peaks of the vibrations of Fe-O and Mn-O bonds of the spinel structure are observed [21]. The $MnFe_2O_4$@ODA-CPL spectrum clearly shows the successful conjugation/absorption of the drug to the nanoformulation, since the major peaks of the drug, which are analyzed in the Supplementary Information, are displayed [35]. Moreover, the absence of the peak of the free -NH_2 group of ODA at 3300 cm^{-1} indicates the formation of a peptide bond between MNPs and the drug, which is further confirmed using ninhydrin colorimetric analysis (Figure S4, SI) [36]. For $MnFe_2O_4$@ODA-CPL, the free -NH_2 were found to be 0.0087 mg/mL (34.8%), which is a very low percentage compared to that of the initial MNPs (82.8%), further confirming their direct coupling with the drug. UV-vis spectroscopy was also used to determine the percentage of drug-loading in the nanoformulation. After the necessary dilutions, the spectrum of $MnFe_2O_4$@ODA-CPL was obtained in methanol, where the dispersion was uniform and stable, as shown in Figure 4b, while the respective spectra of CPL in various concentrations are given in Figure S5a (SI). Initially, with the help of a reference curve (Figure S5b, SI), the concentration of CPL was calculated and found to be 0.016 mg/mL. The relative amount of CPL was estimated to be ~90.9% *w*/*w* of the total mass of the samples. The high percentage of the drug implies that, apart from the direct conjugation, absorption into the double layer of ODA took also place. The TGA curve given in Figure S6a (SI) verifies the presence of various organic layers, including drug and ODA molecules, reaching a final percentage of 75%, while the corrected M_s value of the nanoformulation was found to be equal to 17 emu/g (Figure S6b, SI). The magnetic properties were further supported by magnetic separation of the MNPs-CPL with the aid of a permanent magnet (Figure S9, SI). The increase in hydrodynamic size in the case of the functionalized $MnFe_2O_4$@ODA-CPL compared to the primary MNPs also implies that the functionalization process was successful. Specifically, the nanoformulation has a hydrodynamic size of 292 nm (0.06), which is almost three times higher compared to the $MnFe_2O_4$@ODA MNPs. The zeta potential value for $MnFe_2O_4$@ODA-CPL MNPs at concentrations of 0.25 mg/mL was found to be 15.32 mV, respectively, indicating a stable colloidal dispersion [37].

2.4. Loading of CPL onto PEGylated $MnFe_2O_4$ MNPs

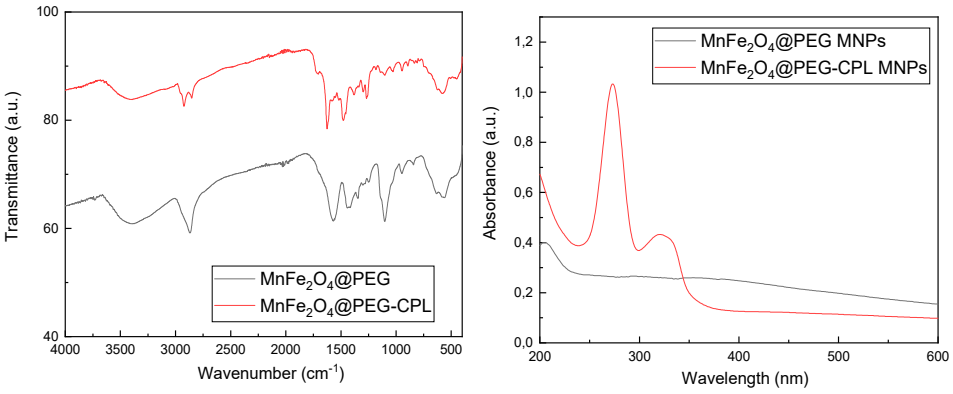
The PEGylated MNPs were loaded with ciprofloxacin upon following a simple post-synthetic procedure, which includes the formation of stable colloidal dispersion and sonication upon the addition of the antibiotic. The successful loading was certified using FT-IR and UV-vis spectroscopy. The FT-IR spectra of the primary PEGylated MNPs and the magnetic nanocarrier $MnFe_2O_4$@PEG-CPL are presented in Figure 5a. The peaks at 2923 and 2853 cm^{-1} are indicative of aliphatic C-H and N-C stretches, respectively, while the observed peaks at 1626 and 1480 cm^{-1} are attributed to the C=O stretch of the carboxyl group and the stretching vibration of C-N in the ciprofloxacin molecules, respectively. The

UV-vis spectrum of the nanocarrier (Figure 5b), apart from verifying the presence of the antibiotic CPL, was used for the calculation of the drug loading percentage, which was found to be 25.1%.



(**a**) (**b**)

Figure 4. (**a**) FT-IR spectra and (**b**) UV-vis spectra of $MnFe_2O_4$@ODA and $MnFe_2O_4$@ODA-CPL MNPs.



(**a**) (**b**)

Figure 5. (**a**) FT-IR spectra and (**b**) UV-vis spectra of $MnFe_2O_4$@PEG and $MnFe_2O_4$@PEG-CPL MNPs.

Bright-field TEM imaging was performed in order to elucidate the morphological features of MNPs before and after the CPL loading. Figure 6a and Figure S7a illustrate $MnFe_2O_4$ nanoparticles embedded in an amorphous matrix of PEG. The MNPs maintain the Fd-3m structure of manganese ferrite in all the cases according to the different selected area electron diffraction patterns from the different MNPs (Figure S7b). The overall morphology is described as a large interconnecting network of MNPs/PEG. The mean size of the nanoparticles was calculated as 12.7 ± 0.6 nm according to the Gaussian fitting given in the size distribution (Figure 6b). The CPL resulted in the partial aggregation of the MNPs in a trapezoid like structure, as displayed in Figure 6c, while other aggregation forms were also observed (Figure S7c,d, SI). The carboxylate groups of CPL can interact with the hydroxyl group of PEG via hydrogen bonding. The hydroxyl groups are highly polar due to the electronegativity difference in hydrogen and oxygen. Thus, they can act both as hydrogen bond donors and acceptors, leading to the mosaic arrangement of the NPs inside the organic matter. However, the loading of CPL induces a significantly smaller size, with a mean size of 10.9 ± 0.6 nm, according to Figure 6d. TEM image of $MnFe_2O_4$@ODA MNPs revealed almost spherical nanoparticles (Figure S8). However, when the CPL was added, no conformational changes were recorded, mainly due to the small size of ODA molecules, which not allow for co-crystallization with other organic molecules, as in the case of PEG, where CPL was enclosed in the PEG matrix.

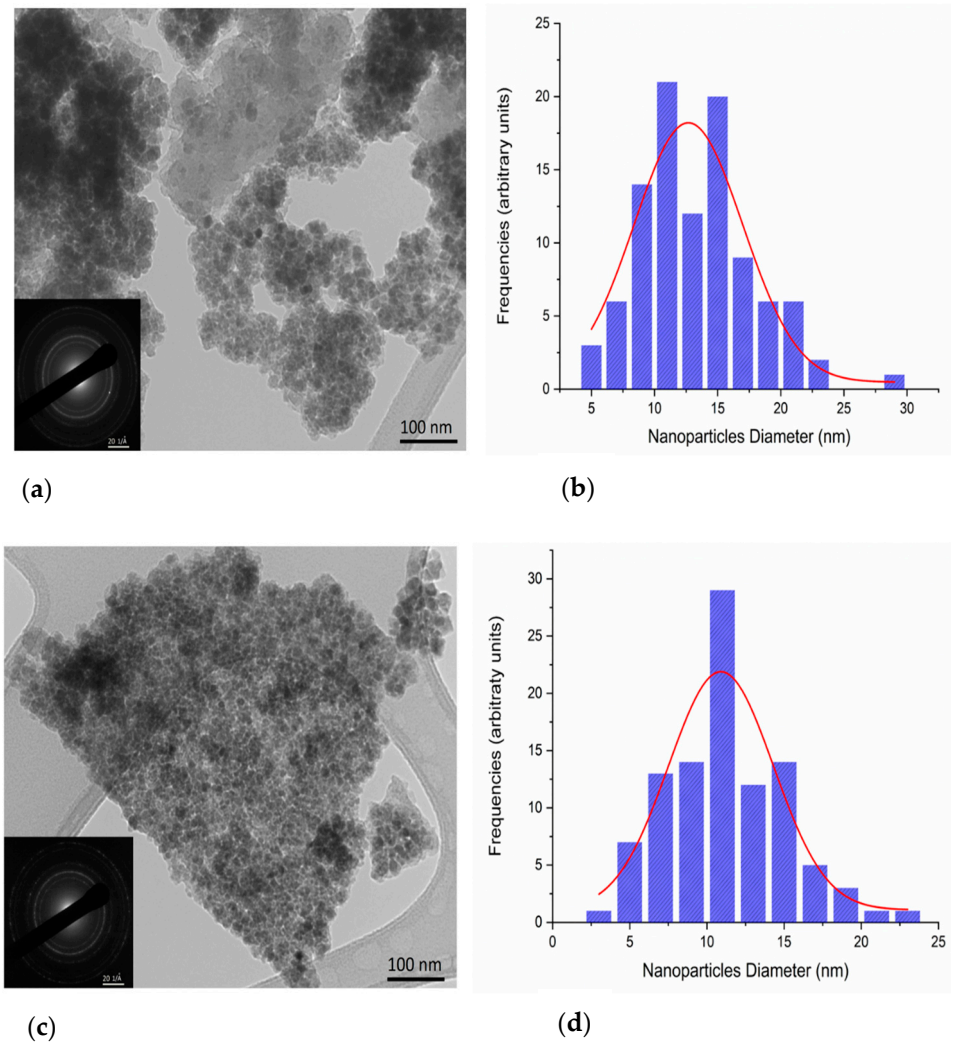


Figure 6. Bright-field TEM image of (**a**) $MnFe_2O_4$@PEG and (**c**) $MnFe_2O_4$@PEG-CPL MNPs with the size distributions at (**b**) and (**d**), respectively. In both TEM images, the corresponding diffraction pattern is depicted as an inset.

2.5. Analysis of Drug Release Studies

Pharmacokinetic studies were conducted to analyze the release mechanism both in the case of antibiotic direct conjugation and loading in the PEG matrix. The data were fitted to zero-order, first-order, Higuchi, and Korsmeyer–Peppas models to find the more suitable one based on the linearity. The results for the nanocarrier $MnFe_2O_4$@ODA-CPL are given in Figure 7, whereas those for $MnFe_2O_4$@PEG-CPL are given in Figure 8. The calculated fitting values R^2 indicate that diffusion better describes the release mechanism in both cases, and, according to the Korsmeyer–Peppas categorization, the non-Fickian anomalous transport takes place, but with a more gradual release profile in the case of the directly conjugated CPL onto the $MnFe_2O_4$@ODA MNPs. In detail, in the case of $MnFe_2O_4$@ODA-CPL nanocarrier, the cumulative ciprofloxacin release after 20 h reached almost 90%, while the respective value for the PEGylated was almost 70%. For the $MnFe_2O_4$@ODA-CPL, the R^2 value derived from the Higuchi model was 0.962 and K_H equal to 13.37, while from the Korsmeyer–Pepas model, R^2 was found to be 0.988 and N (slope) was found to be 0.793. The Higuchi model for the PEGylated nanocarrier of CPL resulted in R^2 = 0.781 and K_H = 9.8, and the Korsmeyer–Pepas model with R^2 = 0.848 and N = 0.633.

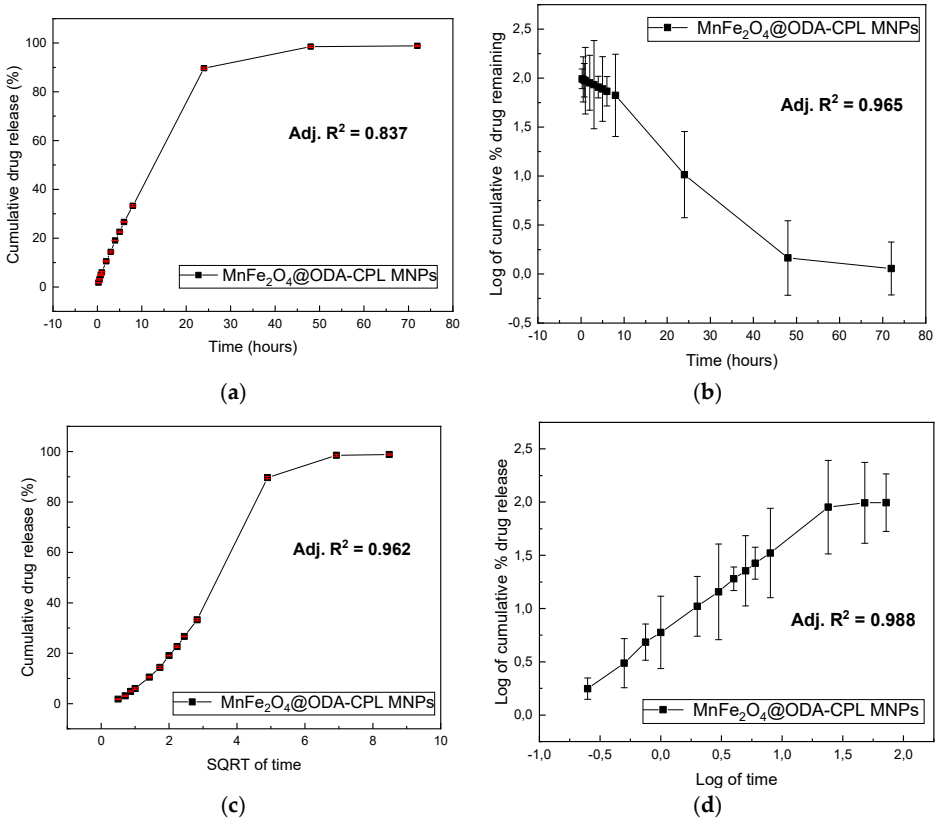


Figure 7. In vitro kinetics for analyzing the release mechanism of CPL from $MnFe_2O_4$@ODA-CPL via (**a**) zero-order, (**b**) first-order, (**c**) Higuchi, and (**d**) Korsmeyer–Peppas models.

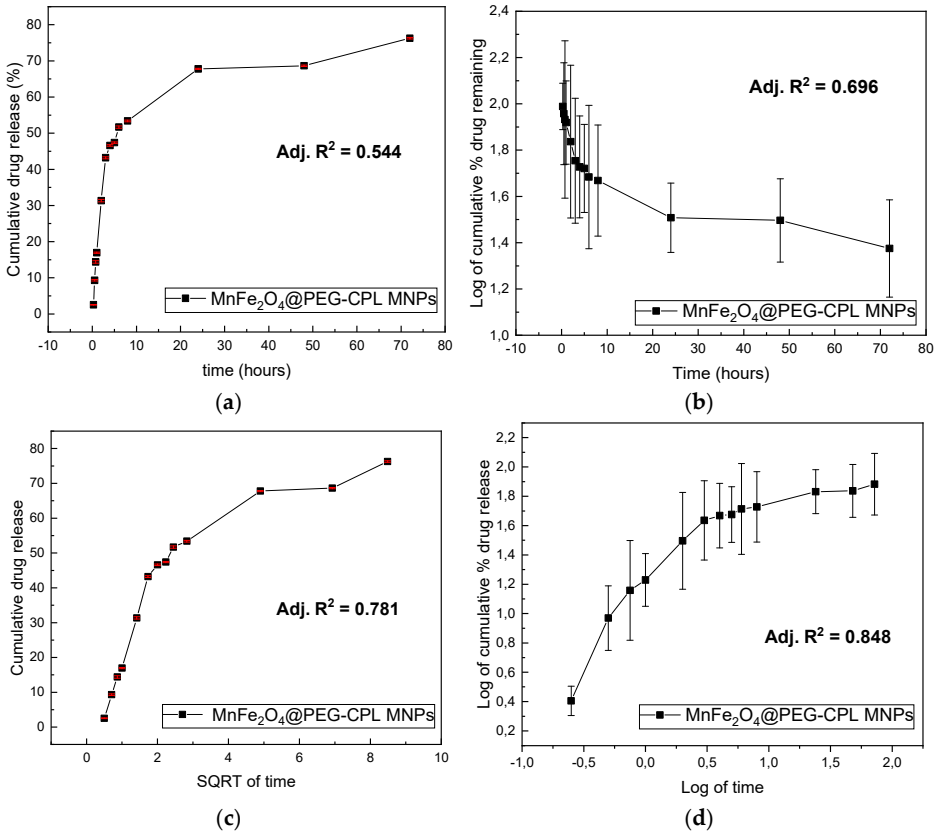


Figure 8. In vitro kinetics for analyzing the release mechanism of CPL from $MnFe_2O_4$@PEG-CPL via (**a**) zero-order, (**b**) first-order, (**c**) Higuchi, and (**d**) Korsmeyer–Peppas models.

2.6. Growth Curves of *P. aeruginosa* in the Presence of CuO, ZnO, CuZn NPs and CPL

As far as the antimicrobial activity is concerned, several methods can be used, such as broth microdilution and standard agar dilution, in order to determine the minimum inhibitory concentration (MIC) and minimum bactericidal concentration (MBC) values [14,38], as well as Checkerboard and time kill assays to reveal the possible synergy between NPs and drugs [39,40]. However, all of these methods are time-consuming and allow for a limited amount of samples to be analyzed at once. The automation of these procedures is a prerequisite when studying multi-drug resistant bacteria with a high prevalence percentage, in order to catch up with the rigorous rhythm of plasmid transfections [2]. Since the BacT/ALERT®3D instrument was used for the first time, initially we proceeded to the evaluation of previously studied NPs using conventional methods. Those coated NPs were found to be effective against the multidrug-resistant clinical strains of *Pseudomonas aeruginosa*, either alone or in a cocktail form with ciprofloxacin (CPL). The concentration of the CuO@PEG, ZnO@PEG, CuZn@TrEG NPs, and the antibiotic was fixed at 25 μg/mL and MIC/4, respectively, based on our previous study concerning the potential role of NPs as efflux pump inhibitors [13]. All of the NPs displayed an almost spherical shape, while their sizes were found to be 15, 35, and 21 nm for CuO, ZnO, and CuZn NPs, respectively [13]. The hydrodynamic sizes were found to be similar in the cells' medium (373−397 nm), and the polyol organic coatings of the samples were 22%, 85%, and 45% w/w for CuZn, ZnO, and CuO NPs, respectively [13]. The growth profiles presented in Figure 9 differ significantly among the sole NPs, the neat CPL, and the cocktail of those. In detail, in the case of sole NPs, the levels of CO_2 reach a plateau almost in the same time point, approximately in a period of 8 h, as in the control culture of *P. aeruginosa*. However, the neat antibiotic led the culture to a steady state in the second day, with the lag phase lasting longer, while in the cases of co-administration, the CO_2 levels became balanced even later, between the middle of the second and the beginning of the third day. It is worth mentioning that, in all cases, the duration of the exponential phase seems to be the same, while the lag phase delayed by the most in the cocktail of CuZn bimetallic NPs with CPL. Sometimes, the total amount of carbon dioxide continued to rise slowly, as in the case of CuZn NPs, due to their endogenous metabolism [41].

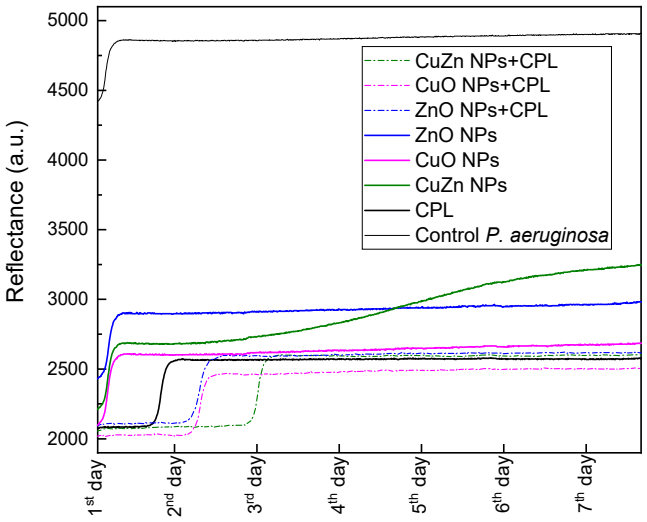


Figure 9. *P. aeruginosa* growth curves using BacT/ALERT®3D in terms of reflectance, corresponding to the produced CO_2 in the presence of the nano-oxides CuO, ZnO, and the bimetallic CuZn NPs, or in the co-administration of the NPs with CPL.

The numerical results show that, among the neat NPs, CuO NPs inhibited the bacterial growth the most (~46%), almost reaching the efficacy of the neat CPL (~47%). In the case of the co-administration of the NPs with CPL, the bacterial growth becomes even more restricted, with the effect being more prominent for the CuO NPs (showing an inhibition of ~49%). However, a larger delay in the lag phase is recorded for the cocktail of CuZn NPs with CPL. These results are in agreement with those presented in our previous study concerning their synergistic activity [13], highlighting the manner of the applicability of the BacT/ALERT®3D system for those kind of measurements.

2.7. Antibacterial Activity of the MNPs Directly Coupled with CPL Towards Multi-Resistant P. aeruginosa

Since the antibacterial activity towards a multidrug-resistant strain is crucial to study in the presence of high concentrations of the antibiotic, we proceeded to the antibacterial activity of the manganese ferrite nanoparticles directly coupled with CPL (~90%). The growth profile of the pseudomonas strain in the presence of the magnetic nanocarrier of ciprofloxacin is presented in Figure 10, while the respective profiles of $MnFe_2O_4$@ODA MNPs, neat CPL, and the cocktail of the MNPs with CPL are also included for comparison reasons. The concentrations included in the experiment were 25 μg/mL for the MNPs and MIC/4 for the antibiotic. The sole presence of the MNPs did not affect the structure of the curve as compared to the control culture of *P. aeruginosa*, with the levels of CO_2 reaching a plateau almost at 8 h. The growth inhibition in the case of the sole MNPs was ~36%, while the neat CPL restricted the growth up to ~47%. The co-administration of the antibiotic with the MNPs showed almost the same inhibition value (~48%), but with a slight retardation of the lag phase. In the case of the magnetic nanocarrier, synergetic effects led to the most pronounced inhibition, being ~52%. The growth curve profile exhibited a steeper exponential phase and appeared to be in-between the neat profile of CPL and the respective profile of the cocktail.

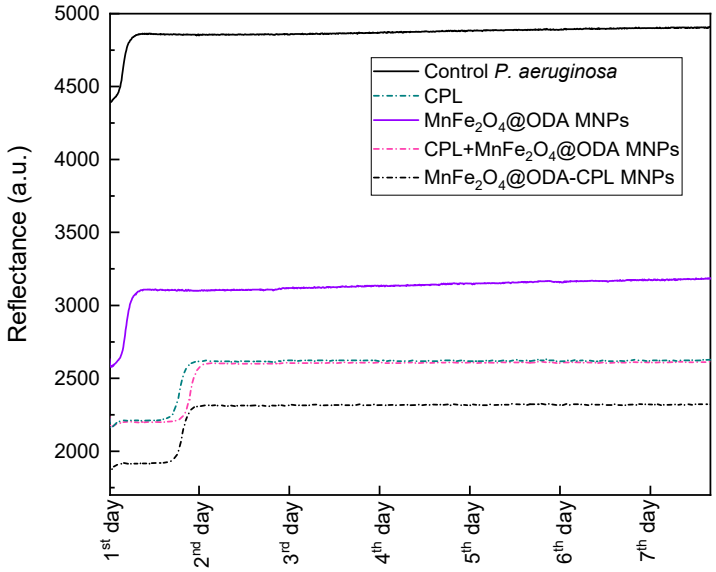


Figure 10. *P. aeruginosa* growth curves by the BacT/ALERT®3D in terms of reflectance corresponding to the produced CO_2 in the presence of $MnFe_2O_4$@ODA MNPs, $MnFe_2O_4$@ODA-CPL MNPs, or in the co-administration of the MNPs with CPL.

The bioefficiency of most antimicrobial agents is often related to their ability to interact with DNA. These agents may cause damage to the DNA's structure, such as fragmentation, causing cell death by apoptosis [42]. In order to analyze further the mechanism of antibacte-

rial activity, the ability of DNA cleavage by $MnFe_2O_4$@ODA MNPs, $MnFe_2O_4$@ODA-CPL MNPs, CPL, and the co-administration of $MnFe_2O_4$@ODA MNPs and CPL at concentrations of 0.5 mg/mL was also under investigation, and the results of the DNA cleavage study are given in Figure 11. DNA cleavage is regulated by the unwinding of the supercoiled plasmid DNA (Form I) to a nicked conformation (Form II) or/and a linear form (Form III). During the separation of circular plasmid DNA using electrophoresis, the supercoiled form moves the fastest [43]. Lane 5 shows untreated plasmid DNA with the supercoiled conformation observed with 78% intensity and the nicked conformation with 22% as a control lane. The progression of the cleavage reaction with $MnFe_2O_4$@ODA MNPs, a cocktail of $MnFe_2O_4$@ODA MNPs and CPL, $MnFe_2O_4$@ODA-CPL MNPs, and CPL is given in Lane 1–4. In particular, $MnFe_2O_4$@ODA MNPs appears not to cause nicks in the double helix of DNA and enhances Form I (Lane 1), while CPL does not affect Form I and causes ds nicks in the double-helix, creating Form III (Lane 4). Their co-administration, as expected, combines the characteristics of both actions, since it causes an amplification of Form I while at the same time creating Form III, but with a lower intensity (Lane 2). Finally, $MnFe_2O_4$@ODA MNPs functionalized with CPL exhibit drug-like activity (Lane 3), leading to the conclusion that these MNPs function as effective nanocarriers of the antibiotic drug CPL.

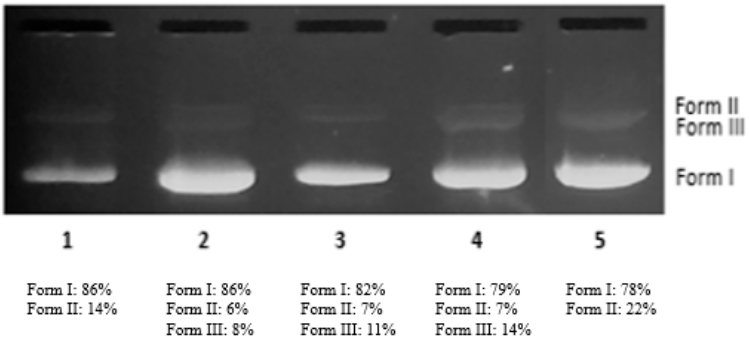


Figure 11. Gel electrophoresis. Lane 1: + $MnFe_2O_4$@ODA MNPs (0.5 mg/mL), Lane 2: DNA + $MnFe_2O_4$@ODA MNPs + CPL (0.5 mg/mL), Lane 3: DNA + $MnFe_2O_4$@ODA-CPL MNPs (0.5 mg/mL), Lane 4: DNA + CPL (0.5 mg/mL), Lane 5: DNA.

3. Materials and Methods

3.1. Materials

All the reagents utilized for our total conducted experiments were analytical grade and were used without any further purification: Iron (III) acetylacetonate $Fe(acac)_3$ (Fluka, Honeywell Research Chemicals, Charlotte, NC, USA, M = 353.17 g/mol), octadecylamine ODA (Fluka, Honeywell Research Chemicals, Charlotte, NC, USA, M = 269.51 g/mol), manganese (III) acetylacetonate hydrated (Sigma-Aldrich, St. Louis, MO, USA, M = 289.15 g/mol), dimethyl sulfoxide DMSO (Chemlab, Zedelgem, Belgium, >99.9%), Chloroform $CHCl_3$ (VWR Chemicals BDH, Avantor, Inc., Radnor, PA, USA 99.2%) (dimethylaminopropyl)-3-ethylcarbodiimide hydrochloride, EDC (TCI, Tokyo Chemical Industry, Tokyo, Japan, >98.0%), triethylamine (Et_3N, $\geq$99.5%), nhydroxysuccinimide NHS (Sigma-Aldrich, St. Louis, MO, USA, 98.0%), ciprofloxacin CPL (Glentham Life Sciences, Corsham, Wiltshire, UK, M = 331.30 g/mol), sodium chloride NaCl (Merck, Darmstadt, Germany), trisodium citrate dihydrate (Merck, Darmstadt, Germany, M = 294.10 g/mol), Phosphate-Buffered Saline, PBS (Glentham Life Sciences, Corsham, Wiltshire, UK, pH 7.4), a Pur-A-Lyzer Midi 1000 Dialysis Kit (Sigma-Aldrich, St. Louis, MO, USA), and deoxyribonucleic acid sodium salt from calf thymus (Sigma-Aldrich, St. Louis, MO, USA). The tested microorganism is a MDR clinical strain of *Pseudomonas aeruginosa* from the Microbiology Laboratory of the University General Hospital of Thessaloniki, AHEPA.

The stock solution of CT DNA was prepared via the dilution of CT DNA to a buffer solution (containing 150 mM NaCl and 15 mM trisodium citrate at pH 7.0) followed by exhaustive stirring, and it was kept at 4 °C for no longer than two weeks. The purity of the stock solution was determined using measurements of the UV absorbance at 260 and 280 nm (A_{260}/A_{280}). A typical ratio of A_{260}/A_{280}, which indicates the absence of protein contamination in a DNA solution, was between 1.7 and 2.0. The DNA concentration was calculated using Lambert Beer's law using molar absorption coefficient ε = 6600 $M^{-1}cm^{-1}$ for the UV absorbance at 260 nm after 1:20 dilution.

3.2. Nanoparticle Synthesis ($MnFe_2O_4$@OAm, $MnFe_2O_4$@ODA, and $MnFe_2O_4$@PEG MNPs)

A typical synthetic process for the solvothermal synthesis of $MnFe_2O_4$ MNPs involves the decomposition of acetylacetonate iron (III) and acetylacetonate manganese (III) precursors at a 2:1 ratio. In detail, 1.8 mmol $Fe(acac)_3$ (0.636 g) and 0.9 mmol $Mn(acac)_3$ (0.317 g) were mixed and dissolved in the sole presence of either OAm (14 mL), ODA (14 mmol), or in PEG8000 (7.5 g). The resulting precursors' solution was magnetically stirred under mild heat until homogenization occurred and then was transferred into a Teflon container (autoclave). The temperature was set to 200 °C (ramp time = 4 °C/min). After 24 h of reactions, the autoclave was left to cool down to room temperature with a rate of 5 °C/min, and $MnFe_2O_4$ MNPs were isolated at first using an external magnet, while repeated washing cycles with EtOH were followed and centrifugation (5000 rpm) was used to remove any byproducts and unreacted precursors.

3.3. Functionalization of $MnFe_2O_4$ MNPs with CPL

3.3.1. Direct Coupling of CPL

A simple functionalization post-synthetic method was carried out for the direct coupling of ciprofloxacin with the MNPs via the free amines presented on their surface. The direct coupling of ciprofloxacin onto the MNPs was achieved according to our previously reported procedure [19], where 20 mg of MNPs were mixed with EDC (47.9 mg), NHS (~3 mg), CPL (82.7 mg), and Et_3N (0.1 mL) in $CHCl_3$ (5 mL). The mixture was shaken vigorously for 24 h, and the MNPs-CPL were collected using repeated cycles of centrifugation and washing with EtOH.

3.3.2. Loading of CPL in the PEG Matrix

In total, 20 mg of $MnFe_2O_4$@PEG MNPs were dispersed in 20 mL chloroform, and 19.5 mg of CPL were added in the above dispersion. This mixture was sonicated for 2 h by keeping the temperature in 25 °C, and the MNPs-CPL were collected using repeated cycles of centrifugation and washing with EtOH.

3.4. Characterization of Nps and Bacterial Growth Curves

Powder X-ray diffraction (XRD) was carried out using a 2-cycle Rigaku $Ultim_{a+}$ diffractometer (40 kV, 30 mA, Cu-K_α radiation). Fourier transform infrared spectra (FTIR) were obtained using a Nicolet™ iS20 FTIR Spectrometer (Thermo Fisher Scientific Inc., Waltham, MA, USA). The spectra were recorded at the wavenumber range of 400–4000 cm^{-1} and are presented after baseline correction and normalization. UV-VIS absorption spectra in methanol were acquired with the aid of a Hitachi U-2001 UV/Vis Spectrophotometer. Transmission electron microscopy (TEM) imaging was performed in the JEOL 2100 LaB TEM (JEOL Ltd., Tokyo, Japan) operated at 200 kV. MNPs were dispersed in methanol and ultrasonicated for 15 min in total. Three droplets of the dispersion were deposited in a TED PELLA lacey Carbon grid and left to dry at room temperature. The diameter of 100 nanoparticles from each sample was measured using a Gatan Digital Micrograph to perform a size distribution analysis. Thermogravimetric analysis (TGA) was performed

using SETA-RAM SetSys-1200 (KEP Technologies, Caluire, France) under N_2 atmosphere, from room temperature to 800 °C with a heating rate of 10 °C min^{-1}. Magnetic measurements were acquired using a vibrating sample magnetometer (1.2H/CF/HT Oxford Instruments VSM, Oxford Instruments, Abingdon, Oxfordshire, UK). The hydrodynamic size, polydispersity index (PDI), and zeta potential of samples were investigated using a particle size analyzer, Litesizer 500 (Anton Paar GmbH, Graz, Austria). The cyclic dichroism spectra were obtained using a Chirascan qCD spectrophotometer (Applied Photophysics, Surrey, UK) with a 0.5 mm thick cell. The bacterial growth curves were performed using a BacT/ALERT®3D instrument (Biogenea Pharmaceuticals Ltd., Thessaloniki, Greece) [44].

3.5. Drug Release Studies

For the drug release study, the dialysis bag approach was followed. In total, 2mg/mL colloidal dispersions of magnetic nanocarriers were prepared, and 200 μL from that dispersion were placed into a Pur-A-Lyzer Midi 1000 dialysis membrane. The membrane floated in 45 mL of PBS pH 7.4 and was shaken (200 rpm) at 35 °C. In certain time intervals, 2 mL of the medium were removed and replaced with a fresh PBS solution. This procedure was followed for both $MnFe_2O_4$@ODA-CPL and $MnFe_2O_4$@PEG-CPL nanocarriers. UV measurements were recorded at 270 nm, and the cumulative release in percentage (Q%) was calculated and plotted against time by setting the absorbance value to 100%, which corresponds to the maximum concentration of the released magnetic nanocarrier in the PBS (c = 0.0088 mg/mL).

3.6. Interaction of NPs with CT-DNA

3.6.1. Ultraviolet–Visible (UV-VIS) Spectroscopy

For this study, stock solutions of $MnFe_2O_4$@OAm, $MnFe_2O_4$@PEG, and $MnFe_2O_4$@ODA were prepared at concentrations of 0.25 mg/mL in DMSO. Absorption UV-VIS spectra were recorded first in a constant DNA concentration (170 μM) and then after varying $MnFe_2O_4$ NPs concentrations (0.6–17 μg/mL). Based on the following Equation (1), it is possible to calculate the binding constant K_b for the CT-DNA-MNPs interaction:

$$\frac{1}{(A - A_0)} = \frac{1}{(A_\infty - A_0)} + \frac{1}{K_b(A_\infty - A_0)[MNPs]} \quad (1)$$

Here, A is the absorbance of the sample having different concentrations of MNPs, A_∞ is the final absorbance of the complex CT-DNA-MNPs, and A_o is the absorbance of CT-DNA at 260 nm in the absence of MNPs. The value of K_b was obtained from the linear relationship between $1/(A - A_0)$ versus 1/[MNPs], where the intercept is equal to $1/(A_\infty - A_0)$ and the slope is equal to $1/K_b(A_\infty - A_0)$ [45].

3.6.2. Circular Dichroism (CD) Studies

A stock solution of $MnFe_2O_4$@OAm MNPs was prepared at a concentration of 1.0 mg/mL in DMSO. CD spectra were recorded first in a constant DNA concentration (1×10^{-3} M) and then upon varying $MnFe_2O_4$ NPs concentrations (25–70 μg/mL). First, a CD spectrum was corrected for a citrate buffer (pH 7.0) signal and then the results were recorded as shown in Figure S2 in the Supplementary Information.

3.7. Interaction of NPs with Plasmid DNA

DNA Cleavage Study Using Gel Electrophoresis

$MnFe_2O_4$@ODA MNPs, $MnFe_2O_4$@ODA-CPL MNPs, CPL, and a cocktail of them were mixed with pBR322 plasmid DNA and Tris buffer (25 μM, pH 6.8) under dark conditions with a total volume of 20 μL in Eppendorf vials. The reaction mixtures were centrifuged

and then incubated for 30 min at 37 °C. After the addition of the gel-loading buffer (6X Orange DNA Loading Dye 10 mM Tris-HCl (pH 7.6), 0.15% orange G, 0.03% xylene cyanol FF, 60% glycerol, and 60 mM EDTA, by Fermentas), the reaction mixtures were loaded on a 1% agarose gel with EB staining. The electrophoresis tank was attached to a power supply at a constant current (65 V for 1 h). The gel was visualized using a 312 nm UV transilluminator and photographed using an FB-PBC-34 camera vilber lourmat. The quantitation of DNA-cleaving activities was performed by the integration of the optical density as a function of the band area using the program "Image J", available at the following website: https://imagej.net/ij/download.html (accessed on 12 February 2025) [46].

4. Conclusions

In the present study, magnetic nanocarriers of ciprofloxacin were prepared and proposed with the prospect of improving the action time and delivery efficiency of the antibiotic ciprofloxacin in order to face multi-resistant bacteria. In the sole presence of aliphatic amines, we managed to simplify the synthetic procedure and isolate $MnFe_2O_4$ MNPs with a large percentage of free amines, while PEGylated MNPs were also prepared. All the primary coated MNPs were found to be biocompatible when studying their interaction with CT-DNA. The direct drug conjugation was found to be more effective (~90%) via the formation of peptide bonds between the CPL carboxylate donor and the free amines of ODA molecules that covered the surface of MNPs. On the other hand, the antibiotic loading in the PEG matrix resulted in only 20% of CPL with an aggregate self-assembly morphology of the $MnFe_2O_4$ nanoparticles. The antimicrobial behavior of the magnetic nanocarriers was for the first time reported using automated microbial growth and detection technology. The magnetic nanocarriers $MnFe_2O_4$@ODA-CPL restricted the growth of multidrug resistant *P. aeruginosa* more effectively than the neat CPL, also giving allowing for the magnetic targeting of the antibiotic to the desired area. Apart from the synergy effects noticed, the magnetic nanocarrier acted as the sole drug in the interactions with plasmid DNA. It is important to denote the use of the automatic BacT/ALERT®3D system for the evaluation of the antimicrobial efficacy of the MNPs. The applicability of this method was verified upon using NPs with known values (found using the Checkerboard method) towards the same strain. Hopefully, this advanced system could lead to innovative evaluations of the activity of other promising nanoparticles.

Supplementary Materials: The following supporting information can be downloaded at: https://www.mdpi.com/article/10.3390/inorganics13020058/s1, Figure S1: FT-IR spectra of (a) MnFe2O4@OAm and (b) MnFe2O4@PEG MNPs; Figure S2: CD spectra of CT-DNA (1×10^{-3} M) on addition of MnFe2O4@OAm MNPs (25–70 μg/ml); Figure S3: FT-IR spectrum of neat ciprofloxacin; Figure S4: Ninhydrin colorimetric analyses before and after direct coupling of MnFe2O4@ODA MNPs and CPL; Figure S5: (a) UV-Vis Absorption spectra for a range of concentrations of ciprofloxacin in methanol, (b) Reference curve for ciprofloxacin; Figure S6: (a) TGA curve of MnFe2O4@ODA-CPL MNPs, (b) VSM measurement of MnFe2O4@ODA-CPL MNPs; Figure S7: (a) Bright-field TEM image of nanoflower chain composed of MnFe2O4@PEG MNPs and (b) the corresponding selected area electron diffraction confirming the Fd-3m structure of manganese ferrite. (c) Bright-field TEM image of nanoflower chain composed of MnFe2O4@PEG-CPL MNPs and (d) magnified image illustrating the morphology of the coated MNPs; Figure S8: (a) TEM image of MnFe2O4@ODA MNPs; Figure S9: The response of the MnFe2O4@ODA-CPL MNPs in the presence of a permanent magnet.

Author Contributions: Conceptualization and writing—original draft preparation, K.G.; writing—reviewing and editing, C.D.-S., K.G. and E.Z. performed the synthesis, post-synthetic procedures, all biological assays, and analysis of the results under the supervision of C.D.-S. and I.M.O. performed TEM observations and the corresponding analysis under the supervision of V.N.

The CEO of Biogenea pharmaceuticals Ltd., N.G., gave access to the automatic microbial detection system, BacT/ALERT®3D, and supported us with the acquirement of the measurements and the analysis of the results with the aid and supervision of I.S.V. All authors have read and agreed to the published version of the manuscript.

Funding: This research work was supported by the Special account for research funds of Aristotle University of Thessaloniki (ELKE, AUTH) under the postdoctoral Fellowship grant (no. 113950/2022). V.N. and I.M.O. acknowledge support from the European Union's Horizon 2020 research and innovation program under Agreement No. 956813. This work was supported by the Taighde Éireann—Research Ireland research centers AMBER (12/RC/2278_P2) and I-Form (21/RC/10295_P2).

Data Availability Statement: The data presented in this study are available in this article.

Acknowledgments: Authors wish to thank the Advanced Microscopy Laboratory (AML) for the provision of their facilities.

Conflicts of Interest: Author Nikolaos Grigoriadis was employed by the company Biogenea pharmaceuticals Ltd. The remaining authors declare that the research was conducted in the absence of any commercial or financial relationships that could be construed as a potential conflict of interest.

References

1. European Centre for Disease Prevention and Control. *Assessing the Health Burden of Infections with Antibiotic-Resistant Bacteria in the EU/EEA, 2016–2020*; ECDC: Stockholm, Sweden, 2022.
2. Kolář, M.; Urbánek, K.; Látal, T. Antibiotic selective pressure and development of bacterial resistance. *Int. J. Antimicrob. Agents* **2001**, *17*, 357–363. [CrossRef] [PubMed]
3. Rice, L.B. The clinical consequences of antimicrobial resistance. *Curr. Opin. Microbiol.* **2009**, *12*, 476–481. [CrossRef] [PubMed]
4. Altun, E.; Aydogdu, M.O.; Chung, E.; Ren, G.; Homer-Vanniasinkam, S.; Edirisinghe, M. Metal-based nanoparticles for combating antibiotic resistance. *Appl. Phys. Rev.* **2021**, *8*, 041303. [CrossRef]
5. Matlock, A.; Garcia, J.A.; Moussavi, K.; Long, B.; Liang, S.Y.-T. Advances in novel antibiotics to treat multidrug-resistant gram-negative bacterial infections. *Intern. Emerg. Med.* **2021**, *16*, 2231–2241. [CrossRef] [PubMed]
6. Pang, Z.; Raudonis, R.; Glick, B.R.; Lin, T.-J.; Cheng, Z. Antibiotic resistance in *Pseudomonas aeruginosa*: Mechanisms and alternative therapeutic strategies. *Biotechnol. Adv.* **2019**, *37*, 177–192. [CrossRef]
7. Aflakian, F.; Mirzavi, F.; Aiyelabegan, H.T.; Soleimani, A.; Navashenaq, J.G.; Karimi-Sani, I.; Zomorodi, A.R.; Vakili-Ghartavol, R. Nanoparticles-based therapeutics for the management of bacterial infections: A special emphasis on FDA approved products and clinical trials. *Eur. J. Pharm. Sci.* **2023**, *188*, 106515. [CrossRef]
8. Himanshu; Mukherjee, R.; Vidic, J.; Leal, E.; da Costa, A.C.; Prudencio, C.R.; Raj, V.S.; Chang, C.-M.; Pandey, R.P. Nanobiotics and the One Health Approach: Boosting the Fight against Antimicrobial Resistance at the Nanoscale. *Biomolecules* **2023**, *13*, 1182. [CrossRef]
9. Gautam, S.; Das, D.K.; Kaur, J.; Kumar, A.; Ubaidullah, M.; Hasan, M.; Yadav, K.K.; Gupta, R.K. Transition metal-based nanoparticles as potential antimicrobial agents: Recent advancements, mechanistic, challenges, and future prospects. *Discov. Nano* **2023**, *18*, 84. [CrossRef]
10. Mamun, M.M.; Sorinolu, A.J.; Munir, M.; Vejerano, E.P. Nanoantibiotics: Functions and Properties at the Nanoscale to Combat Antibiotic Resistance. *Front. Chem.* **2021**, *9*, 687660. [CrossRef]
11. Turabik, M.; Özdemir, S.; Akinbingol, G.; Gonca, S.; Gecgel, C. Comparison of antioxidant, antimicrobial, DNA cleavage, cell viability, and biofilm inhibition activities of mono- and bimetallic copper and zinc nanoparticles. *Inorg. Chem. Commun.* **2023**, *155*, 111072. [CrossRef]
12. Badry, A.; Ibrahim, A.A.E.H.; Said, M.I.; Nasr, A.A.E.; Mohamed, M.A.; Hassan, A.K.; Safwat, M.M. In vitro assessment of PEG-6000 coated-ZnO nanoparticles: Modulating action to the resisted antibiotic activity against APEC. *BMC Vet. Res.* **2023**, *19*, 1. [CrossRef] [PubMed]
13. Eleftheriadou, I.; Giannousi, K.; Protonotariou, E.; Skoura, L.; Arsenakis, M.; Dendrinou-Samara, C.; Sivropoulou, A. Cocktail of CuO, ZnO, or CuZn Nanoparticles and Antibiotics for Combating Multidrug-Resistant *Pseudomonas aeruginosa* via Efflux Pump Inhibition. *ACS Appl. Nano Mater.* **2021**, *4*, 9799–9810. [CrossRef]
14. Venter, H.; Mowla, R.; Ohene-Agyei, T.; Ma, S. RND-type drug efflux pumps from Gram-negative bacteria: Molecular mechanism and inhibition. *Front. Microbiol.* **2015**, *6*, 377. [CrossRef] [PubMed]
15. Mu, H.; Tang, J.; Liu, Q.; Sun, C.; Wang, T.; Duan, J. Potent Antibacterial Nanoparticles against Biofilm and Intracellular Bacteria. *Sci. Rep.* **2016**, *6*, 18877. [CrossRef]

16. Lai, H.-Z.; Chen, W.-Y.; Wu, C.-Y.; Chen, Y.-C. Potent Antibacterial Nanoparticles for Pathogenic Bacteria. *ACS Appl. Mater. Interfaces* **2015**, *7*, 2046–2054. [CrossRef]
17. Kudr, J.; Haddad, Y.; Richtera, L.; Heger, Z.; Cernak, M.; Adam, V.; Zitka, O. Magnetic Nanoparticles: From Design and Synthesis to Real World Applications. *Nanomaterials* **2017**, *7*, 243. [CrossRef]
18. Na, H.B.; Song, I.C.; Hyeon, T. Inorganic Nanoparticles for MRI Contrast Agents. *Adv. Mater.* **2009**, *21*, 2133–2148. [CrossRef]
19. Hoshyar, N.; Gray, S.; Han, H.; Bao, G. The effect of nanoparticle size on in vivo pharmacokinetics and cellular interaction. *Nanomedicine* **2016**, *11*, 673–692. [CrossRef]
20. Wang, G.; Zhao, D.; Ma, Y.; Zhang, Z.; Che, H.; Mu, J.; Zhang, X.; Zhang, Z. Synthesis and characterization of polymer-coated manganese ferrite nanoparticles as controlled drug delivery. *Appl. Surf. Sci.* **2018**, *428*, 258–263. [CrossRef]
21. Giannousi, K.; Koutroumpis, E.; Georgiadou, V.; Karagkounis, V.; Dendrinou-Samara, C. Nanoplatforms of Manganese Ferrite Nanoparticles Functionalized with Anti-Inflammatory Drugs. *Eur. J. Inorg. Chem.* **2019**, *2019*, 1895–1903. [CrossRef]
22. Phalake, S.S.; Somvanshi, S.B.; Tofail, S.A.M.; Thorat, N.D.; Khot, V.M. Functionalized manganese iron oxide nanoparticles: A dual potential magneto-chemotherapeutic cargo in a 3D breast cancer model. *Nanoscale* **2023**, *15*, 15686–15699. [CrossRef] [PubMed]
23. Ribeiro, A.I.; Dias, A.M.; Zille, A. Synergistic Effects Between Metal Nanoparticles and Commercial Antimicrobial Agents: A Review. *ACS Appl. Nano Mater.* **2022**, *5*, 3030–3064. [CrossRef] [PubMed]
24. Baquero, F.; Levin, B. Proximate and ultimate causes of the bactericidal action of antibiotics. *Nat. Rev. Microbiol.* **2021**, *19*, 123–132. [CrossRef] [PubMed]
25. Rehman, A.; Patrick, W.M.; Lamont, I.L. Mechanisms of ciprofloxacin resistance in *Pseudomonas aeruginosa*: New approaches to an old problem. *J. Med. Microbiol.* **2019**, *68*, 1–10. [CrossRef] [PubMed]
26. Seegmuller, I.; Eschenbach, U.; Kamereck, K. Sensitivity of the BACT/ALERT® FA medium for detection of *Pseudomonas aeruginosa* in pre-incubated blood cultures and its temperature dependence. *J. Med. Microbiol.* **2004**, *53*, 869–874. [CrossRef]
27. Vamvakidis, K.; Katsikini, M.; Sakellari, D.; Paloura, E.C.; Kalogirou, O.; Dendrinou-Samara, C. Reducing the inversion degree of $MnFe_2O_4$ nanoparticles through synthesis to enhance magnetization: Evaluation of their 1H NMR relaxation and heating efficiency. *Dalton Trans.* **2014**, *43*, 12754–12765. [CrossRef]
28. Vamvakidis, K.; Katsikini, M.; Vourlias, G.; Angelakeris, M.; Paloura, E.C.; Dendrinou-Samara, C. Composition and hydrophilicity control of Mn-doped ferrite ($Mn_xFe_{3-x}O_4$) nanoparticles induced by polyol differentiation. *Dalton Trans.* **2015**, *44*, 5396–5406. [CrossRef]
29. Khan, S.; Cho, W.C.; Jaragh-Alhadad, L.A.; Tarharoudi, R.; Bloukh, S.H.; Edis, Z.; Sari, S.; Falahati, M.; Hagen, T.L.T.; Khan, R.H.; et al. Nano-bio interaction: An overview on the biochemical binding of DNA to inorganic nanoparticles for the development of anticancer and antibacterial nano-platforms. *Int. J. Biol. Macromol.* **2023**, *225*, 544–556. [CrossRef]
30. Olson, N.D.; Morrow, J.B. DNA extract characterization process for microbial detection methods development and validation. *BMC Res. Notes* **2012**, *5*, 668. [CrossRef]
31. Sonia, K.; Kukreti, S.; Kaushik, M. Exploring the potential of environment friendly silver nanoparticles for DNA interaction: Physicochemical approach. *J. Photochem. Photobiol. B Biol.* **2019**, *194*, 158–165. [CrossRef]
32. Yadav, N.; Singh, A.; Kaushik, M. Hydrothermal synthesis and characterization of magnetic Fe_3O_4 and APTS coated Fe_3O_4 nanoparticles: Physicochemical investigations of interaction with DNA. *J. Mater. Sci. Mater. Med.* **2020**, *31*, 68. [CrossRef] [PubMed]
33. Kong, D.-M.; Wang, J.; Zhu, L.-N.; Jin, Y.-W.; Li, X.-Z.; Shen, H.-X.; Mi, H.-F. Oxidative DNA cleavage by Schiff base tetraaza-macrocyclic oxamido nickel(II) complexes, *J. Inorg. Biochem.* **2008**, *102*, 824–832. [CrossRef] [PubMed]
34. Kaur, G.; Dogra, V.; Kumar, R.; Kumar, S.; Bhanjana, G.; Dilbaghi, N.; Singhal, N.K. DNA interaction, anti-proliferative effect of copper oxide nanocolloids prepared from metallosurfactant based microemulsions acting as precursor, template and reducing agent. *Int. J. Pharm.* **2018**, *535*, 95–105. [CrossRef] [PubMed]
35. Al-Omar, M.A. Ciprofloxacin: Physical Profile. In *Profiles of Drug Substances, Excipients and Related Methodology*; Brittain, H.G., Ed.; Academic Press: Cambridge, MA, USA, 2005; Volume 31, pp. 163–178, ISBN 9780122608315; ISSN 1871-5125. [CrossRef]
36. Giannousi, K.; Menelaou, M.; Arvanitidis, J.; Angelakeris, M.; Pantazaki, A.; Dendrinou-Samara, C. Hetero-nanocomposites of magnetic and antifungal nanoparticles as a platform for magnetomechanical stress induction in *Saccharomyces cerevisiae*. *J. Mater. Chem. B* **2015**, *3*, 5341–5351. [CrossRef] [PubMed]
37. Islam, K.; Haque, M.; Kumar, A.; Hoq, A.; Hyder, F.; Hoque, S.M. Manganese Ferrite Nanoparticles ($MnFe_2O_4$): Size Dependence for Hyperthermia and Negative/Positive Contrast Enhancement in MRI. *Nanomaterials* **2020**, *10*, 2297. [CrossRef]
38. CLSI. *Performance Standards for Antimicrobial Susceptibility Testing*, 28th ed.; CLSI supplement M100; Clinical and Laboratory Standards Institute: Wayne, PA, USA, 2018.
39. Sopirala, M.M.; Mangino, J.E.; Gebreyes, W.A.; Biller, B.; Bannerman, T.; Balada-Llasat, J.M.; Pancholi, P. Synergy testing by Etest, microdilution checkerboard, and time-kill methods for pan-drug-resistant Acinetobacter baumannii. *Antimicrob. Agents Chemother.* **2010**, *54*, 4678–4683. [CrossRef]

40. National Committee for Clinical Laboratory Standards. *Methods for Determining Bactericidal Activity of Antimicrobial Agents*; Document M26-A; NCCLS: Wayne, PA, USA, 1999.
41. Estrella, M.R.; Brusseau, M.L.; Maier, R.S.; Pepper, I.L.; Wierenga, P.J.; Miller, R.M. Biodegradation, sorption, and transport of 2,4-dichlorophenoxyacetic acid in saturated and unsaturated soils. *Appl. Environ. Microbiol.* **1993**, *59*, 4266–4273. [CrossRef]
42. Hudaverdi, A.; Serpil, G.; Zelal, I.; Özdemir, S.; Yalvac, M.; Dizge, N.; Deepanraj, B.; Ashraf, G.A. Iron Oxide Nanoparticles Synthesis From Vermicomposting Leachate and its Antioxidant Activities. *Front. Mater.* **2022**, *9*, 912066. [CrossRef]
43. Varghese, N.; Jose, J.R.; Krishna, P.M.; Philip, D.; Joy, F.; Vinod, T.P.; Prathapachandra Kurup, M.R.; Nair, Y. *In vitro* Analytical Techniques as Screening Tools to investigate the Metal chelate-DNA interactions. *ChemistrySelect* **2023**, *8*, e202203615. [CrossRef]
44. bioMérieux, Inc. BacT/ALERT® 3D User Manual. 2010. Available online: http://www.frankshospitalworkshop.com/equipment/documents/automated_analyzer/user_manuals/Biomerieux%20Bact-Alert%203D%20-%20User%20Manual.pdf (accessed on 12 February 2025).
45. Shahabadi, N.; Akbari, A.; Karampour, F.; Falsafi, M.; Zendehcheshm, S. *In vitro* cytotoxicity, antibacterial activity and HSA and ct-DNA interaction studies of chlorogenic acid loaded on γ-Fe_2O_3@SiO_2 as new nanoparticles. *J. Biomol. Struct. Dyn.* **2023**, *41*, 2300–2320. [CrossRef]
46. Pasolli, M.; Dafnopoulos, K.; Andreou, N.-P.; Gritzapis, P.S.; Koffa, M.; Koumbis, A.E.; Psomas, G.; Fylaktakidou, K.C. Pyridine and *p*-Nitrophenyl Oxime Esters with Possible Photochemotherapeutic Activity: Synthesis, DNA Photocleavage and DNA Binding Studies. *Molecules* **2016**, *21*, 864. [CrossRef]

Disclaimer/Publisher's Note: The statements, opinions and data contained in all publications are solely those of the individual author(s) and contributor(s) and not of MDPI and/or the editor(s). MDPI and/or the editor(s) disclaim responsibility for any injury to people or property resulting from any ideas, methods, instructions or products referred to in the content.